J. Fluid Mech. (2003), *vol.* 475, *pp.* 1–19.
DOI: 10.1017/S0022112002001957 Printed in the United Kingdom

On the instability of a falling film due to localized heating

By JAN M. SKOTHEIM[1,2], UWE THIELE[1,3] AND BENOIT SCHEID[4]

[1]Instituto Pluridisciplinar, Universidad Complutense, 28040 Madrid, Spain

[2]Department of Applied Mathematics and Theoretical Physics, University of Cambridge, Centre for Mathematical Sciences, Wilberforce Road, Cambridge CB3 0WA, UK

[3]Department of Physics, University of California Berkeley, CA 94720-7300, USA

[4]Microgravity Research Center, Université Libre de Bruxelles, 1050 Brussels, Belgium

(Received 17 October 2000 and in revised form 3 April 2002)

We analyse the stability of a thin film falling under the influence of gravity down a locally heated plate. Marangoni flow, due to local temperature changes influencing the surface tension, opposes the gravitationally driven Poiseuille flow and forms a horizontal band at the upper edge of the heater. The thickness of the band increases with the surface tension gradient, until an instability forms a rivulet structure periodic in the transverse direction. We study the dependence of the critical Marangoni number, a non-dimensional measure of the surface tension gradient at the onset of instability, on the associated Bond and Biot numbers, non-dimensional measures of the curvature pressure and heat-conductive properties of the film respectively. We develop a model based on long-wave theory to calculate base-state solutions and their linear stability. We obtain dispersion relations, which give us the wavelength and growth rate of the fastest growing mode. The calculated film profile and wavelength of the most unstable mode at the instability threshold are in quantitative agreement with the experimental results. We show via an energy analysis of the most unstable linear eigenmode that the instability is driven by gravity and an interaction between base-state curvature and the perturbation thickness. In the case of non-zero Biot number transverse variations of the temperature profile also contribute to destabilization.

1. Introduction

The importance of thin (< 1 mm) liquid films has led to intensive studies of their flow characteristics and stability against rupture. For a recent review of the field see Oron, Davis & Bankoff (1997). The effects of thermocapillarity on gravitationally driven flow in thin liquid layers on a solid support and their stability has been studied both theoretically and experimentally and has applications to coating technology and heat transfer devices (Lin 1974; Sreenivasan & Lin 1978; Kelley, Davis & Goussis 1986; Joo, Davis & Bankoff 1991; Ji & Setterwall 1994; Ito, Masunaga & Baba 1995; Joo, Davis & Bankoff 1996; Zeytounian 1998). Falling film evaporators, used for the separation of temperature-sensitive fluids, rely on the heat-transfer properties and stability of falling thin liquid films. To avoid the reduction of their performance by film breakdown it is of paramount importance to understand when and why instabilities arise that may break the film.

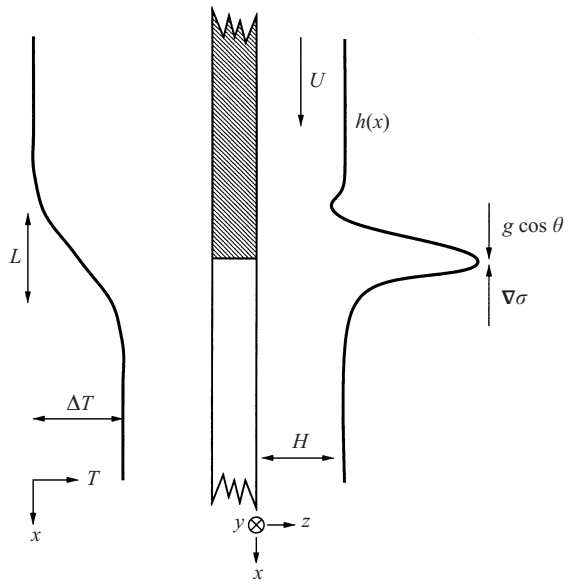

FIGURE 1. Schematic diagram of the problem viewed from the transverse y-direction.

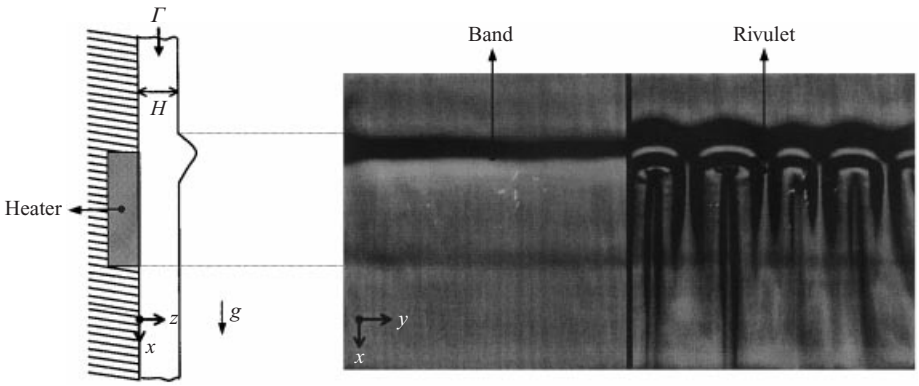

FIGURE 2. Two photographs of the falling film viewed from the z-direction, obtained using shadowgraph techniques. For $Ma^* < Ma_c^*$ the bump forms at the upper edge of the heater (left), whereas for $Ma^* > Ma_c^*$ the rivulet structure appears (right). The solution consists of 25% ethyl alcohol, $Re = 0.25$.

Recent experimental studies have focused on thin films falling down inhomogeneously heated plates and have revealed the occurrence of novel instabilities (Kabov, Marchuk & Chupin 1996; Kabov 1996; Kabov & Chinnov 1997; Kabov 1998; Scheid *et al.* 2000). In this paper we study the stability of low-Reynolds-number Poiseuille flow on a locally heated plate. At the upper edge of the heater the temperature of the plate increases by ΔT within a distance L (see figure 1). As the temperature of the fluid surface increases, the surface tension decreases. The concomitant surface tension gradient produces a Marangoni flow opposed to the gravitationally driven flow. As first reported in Kabov (1994), the competing flows produce a horizontal band of increased film thickness at the upper edge of the heater, which may become unstable and develop rivulets periodic in the direction transverse to the flow. Figure 2 shows

shadowgraph images of the bump development at the upper edge of the heater and the subsequent rivulet instability.

We apply long-wave theory (Oron *et al.* 1997) to derive a nonlinear equation for the film thickness, $h(x)$, of the steady state flow (§ 2). We then solve for the steady film profiles and study the dependence of the system on the associated Marangoni number, a measure of the surface tension gradient, the Bond number, a measure of the curvature pressure, and the Biot number, which measures the heat transfer from the film to the ambient. In order to calculate the solutions using continuation methods we extend our system from a single temperature increase to a periodic array of temperature increases (§ 3). We apply linear stability theory to the steady solutions to find dispersion relations giving us the growth rate of the most unstable mode as a function of the wavenumber in the transverse direction (§ 4). For large periods of the array we recover the experimental situation of one localized heater (§ 5). In § 6 we perform an energy analysis following the method of Spaid & Homsy (1996) to elucidate the physical nature of the instability and to understand its relation to the various fingering instabilities of liquid rims that accompany moving contact lines (Troian *et al.* 1989; Spaid & Homsy 1996; Bertozzi & Brenner 1997; Kataoka & Troian 1997; Bertozzi *et al.* 1998; Kataoka & Troian 1998; Moyle, Chen & Homsy 1999; Eres, Schwartz & Roy 2000). It is worth mentioning that fluid flow over a step change in the substrate topology can also generate stationary fluid ridges (Kalliadasis, Bielarz & Homsy 2000); however, these ridges are found to be strongly stable over a wide range of parameter space (Kalliadasis & Homsy 2001). Another example of a stationary fluid ridge is found when a viscous fluid is placed in a horizontal cylinder rotating about its longitudinal axis (Hosoi & Mahadevan 1999). Using the interpretation of the energy results in the literature, we compare the results to the work of Spaid & Homsy (1996) and Kataoka & Troian (1997, 1998) on moving contact line instabilities. We propose a novel interpretation of the energy analysis, which yields a physical interpretation of the instability mechanism. As one increases the transverse wavenumber, k, of the perturbation the marginally stable state at $k = 0$ is destabilized by both gravity and an interaction between the base-state curvature and the perturbation thickness. An energy analysis of the case of non-zero Biot number reveals a more complex phenomenon containing the additional effect of transverse variations of the temperature profile, which produces a thermocapillary instability. The results are discussed in detail and shown to be in agreement with existing experimental data (§ 7).

2. Mathematical model

In this section we construct a mathematical model for a thin film flowing down a locally heated plate at an angle θ with the vertical (figure 1). We begin with the Navier–Stokes, heat, and continuity equations for incompressible Newtonian fluids:

$$\boldsymbol{u}_t + \boldsymbol{u}\cdot\nabla\boldsymbol{u} = -\frac{\nabla P}{\rho} + \nu\nabla^2\boldsymbol{u} - \boldsymbol{g}, \tag{2.1}$$

$$\rho c(T_t + \boldsymbol{u}\cdot\nabla T) = k_{th}\nabla^2 T, \tag{2.2}$$

$$\nabla\cdot\boldsymbol{u} = 0, \tag{2.3}$$

where ρ, ν, c and k_{th} correspond to the density, kinematic viscosity, specific heat and thermal conductivity of the fluid, $\boldsymbol{u}$ is the velocity field (u, v, w), P is the pressure, $\boldsymbol{g}$ is acceleration due to gravity, T is the temperature field. We have applied the

Non-dimensional group	Symbol	Physical interpretation	Definition	Approximate value
Aspect ratio	ϵ	$\frac{\text{film thickness of unheated flow}}{\text{lengthscale of temperature gradient}}$	$\frac{H}{L}$	10^{-2}
Associated Bond number	Bo^*	$\frac{\text{gravity}}{\text{curvature pressure}}$	$\frac{\rho g L^3 \cos\theta}{H\sigma_0}$	10
Associated Marangoni number	Ma^*	$\frac{\text{surface stress}}{\text{gravity}}$	$\frac{\sigma_T \Delta T}{HL\rho g \cos\theta}$	10
Biot number	Bi	$\frac{\text{heat transfer}}{\text{heat conductivity}}$	$\frac{\alpha_{th} H}{k_{th}}$	0.1
Grashof number	Gr	$\frac{\text{buoyancy force}}{\text{viscous force}}$	$\frac{\alpha \Delta T}{\cos\theta}$	10^{-3}
Péclet number	Pe	$\frac{\text{heat advection}}{\text{heat conduction}}$	$\frac{\rho c g H^3 \cos\theta}{k_{th} \nu}$	10^{-1}
Reynolds number	Re	$\frac{\text{inertia}}{\text{viscosity}}$	$\frac{gH^2 L \cos\theta}{\nu^2}$	1

TABLE 1. Non-dimensional groups and their approximate values.

Boussinesq approximation (Perez Cordon & Velarde 1975), and subscripts t, x, y and z denote derivatives from now on; x is the direction of the flow, and z is the direction perpendicular to the plate. The transverse direction is y (see figure 1). Buoyancy is neglected since the Grashof number is small (see table 1). We integrate the continuity equation (2.3) across the film and apply the kinematic boundary condition at the free surface, $w = h_t + \boldsymbol{u} \cdot \nabla h$, to find an evolution equation for the film thickness, $h(x, y)$:

$$h_t + \nabla \cdot \Gamma = 0, \tag{2.4}$$

where $\Gamma = \int_0^h \boldsymbol{u}\, \mathrm{d}z$ is the flux. We are interested in structure formation on the timescale of the convective motion of the flow and use the velocity scale based on a balance of viscous and gravitational forces. The dimensionless variables (primed) are defined by

$$\left.\begin{array}{lll} x = Lx', & y = Ly', & z = Hz', \\ u = \dfrac{g\cos\theta H^2}{\nu} u', & v = \dfrac{g\cos\theta H^2}{\nu} v', & w = \dfrac{g\cos\theta H^3}{L\nu} w', \\ P - P_a = \rho g L \cos\theta P', & t = \dfrac{L\nu}{g\cos\theta H^2} t', & T - T_\infty = \Delta T\, T', \end{array}\right\} \tag{2.5}$$

where H is the height of the film, L is the lengthscale in the streamwise direction over which the temperature varies, P_a is the ambient pressure, ΔT is the temperature jump at a heater and T_∞ is the ambient temperature *and* the upstream temperature far away from the heater. The experimental parameters can be found in table 2. Applying standard lubrication theory in terms of the parameter $\epsilon = H/L$ yields, after dropping the primes, the leading-order balance:

$$0 = u_{zz} - P_x + 1, \tag{2.6}$$

$$0 = v_{zz} - P_y, \tag{2.7}$$

Physical parameter	Symbol	Approximate value
Density	ρ	$1\,\mathrm{g\,cm^{-3}}$
Kinematic viscosity	v	$10^{-2}\,\mathrm{cm^2\,s^{-1}}$
Surface tension	σ_0	$70\,\mathrm{g\,s^{-2}}$
Film height	H	$10^{-3}\,\mathrm{cm}$
Lengthscale of temperature gradient at the solid	L	$10^{-1}\,\mathrm{cm}$
Velocity in x-direction	U	$10^{-1}\,\mathrm{cm\,s^{-1}}$
Velocity in z-direction	W	$10^{-3}\,\mathrm{cm\,s^{-1}}$
Gravity	g	$10^{3}\,\mathrm{cm\,s^{-2}}$
Sensitivity of surface tension to temperature	σ_T	$10^{-1}\,\mathrm{g\,s^{-2}\,K^{-1}}$
Change in temperature	ΔT	$10\,\mathrm{K}$
Angle of plate from vertical	θ	0
Heat transfer coefficient	α_{th}	$10^{7}\,\mathrm{g\,s^{-3}\,K^{-1}}$
Thermal conductivity	k_{th}	$6\times10^{4}\,\mathrm{g\,cm\,s^{-3}\,K^{-1}}$
Specific heat	c	$4\times10^{7}\,\mathrm{cm^2\,s^{-2}\,K^{-1}}$
Thermal expansion coefficient	α	$3\times10^{-4}\,\mathrm{K^{-1}}$

TABLE 2. Experimental parameters.

$$0 = P_z, \tag{2.8}$$

$$0 = T_{zz}. \tag{2.9}$$

We note that although the Reynolds number, $Re = g\cos\theta H^2 L/v^2$, is approximately 1 (see table 1), the non-dimensional group multiplying the inertial terms in equations (2.6) and (2.7) is $\epsilon^2 Re$. Similarly, the Péclet number in the leading-order balance is multiplied by a factor of ϵ and does not appear in equation (2.8). The asymptotic approximation breaks down when the aspect ratio ϵ is no longer small as is the case for the thickest films investigated in the experiment. To solve the above set of equations we require two boundary conditions for the temperature, four for the velocity field, and one for the pressure. Since the metal heater is a good conductor of heat we can assume that the temperature of the fluid at $z = 0$ can be given by the temperature of the solid surface, $T_0(x)$. The boundary condition on the temperature at the free surface is given by Newton's cooling law. Non-dimensionalizing these boundary conditions on the temperature field yields

$$T = T_0(x) \quad \text{at} \quad z = 0, \tag{2.10}$$

$$0 = T_z + BiT \quad \text{at} \quad z = h(x), \tag{2.11}$$

where Bi is the Biot number. The temperature field at the interface is found by integrating equation (2.8) twice and applying the boundary conditions (2.10) and (2.11):

$$T(x, z = h) = T^i(x) = \frac{T_0(x)}{1 + Bih}. \tag{2.12}$$

We shall assume that surface tension varies linearly with temperature, $\sigma(T) = \sigma_0 - \sigma_T(T - T_\infty)$, and consider fluids where the surface tension decreases with increasing temperature, $\sigma_T > 0$. The appropriate boundary conditions, given here at leading order, for the velocity field are the no-slip condition at the solid–fluid interface and

the tangential and normal stress conditions on the surface:

$$\boldsymbol{u} = 0 \quad \text{at} \quad z = 0, \tag{2.13}$$

$$\boldsymbol{u}_z = -Ma^* \nabla T^i \quad \text{at} \quad z = h(x), \tag{2.14}$$

where the associated Marangoni number, Ma^*, is positive. Table 1 contains definitions and characteristic values of all the non-dimensional groups used in this analysis. The leading-order balance of the normal stress condition at the film surface in non-dimensional form yields the pressure

$$P = -\frac{1}{Bo^*}\nabla^2 h, \tag{2.15}$$

where Bo^* is the associated Bond number. Equations (2.6)–(2.8) can be solved using the boundary conditions (2.10)–(2.15) and the integrated continuity equation (2.4) to find the evolution equation:

$$h_t + \nabla \cdot \left[\frac{h^3}{3} \left(\frac{1}{Bo^*} \nabla \nabla^2 h + \boldsymbol{e}_x \right) - \frac{h^2}{2} Ma^* \nabla T^i \right] = 0, \tag{2.16}$$

where $\boldsymbol{e}_x$ denotes the unit vector in the x-direction.

The essential difference between this evolution equation and similar equations in the literature (Oron & Rosenau 1992; Joo *et al.* 1991) is that the Marangoni effect influences the leading-order balance determining the steady flow. In contrast to Joo *et al.* (1991) equation (2.16) does not contain the aspect ratio ϵ as a parameter.

3. Base state

To calculate the base state we assume that the flow is steady ($h_t = 0$) and has no transverse variation ($v = 0$), and integrate equation (2.16) once to obtain the following nonlinear ordinary differential equation for the steady height profile of the film, to be solved with the far-field boundary condition $h \to 1$ as $x \to \pm\infty$:

$$1 = -\tfrac{3}{2} Ma^* T_x^i h^2 + \left(\frac{1}{Bo^*} h_{xxx} + 1 \right) h^3. \tag{3.1}$$

In order to use continuation techniques for finding solutions of equation (3.1) we choose a periodic temperature gradient at the plate surface:

$$T_{0x}(x) = |\cos(\pi x L/l)| \operatorname{sech}^2 \left[\frac{2l}{\pi L} \sin\left(\pi \frac{xL}{l} \right) \right], \tag{3.2}$$

which corresponds to an infinite array of localized temperature increases. We have now introduced a second lengthscale, l, the period of the array. Unless stated otherwise we compute our results for $l = 20L$. In the limit of infinite l we recover the case of a single temperature increase and the temperature gradient (3.2) reduces to $T_{0x} = \operatorname{sech}^2(2x)$. The periodic solutions of (3.1) with (3.2) are followed through parameter space using the continuation software AUTO (Doedel *et al.* 1997). We start with the flat-film solution at $Ma^* = 0$ for a fixed Bo^* and proceed by increasing Ma^* and Bi to their desired values. As a check we performed the analysis in this paper for a temperature profile T_0 having the shape of an error function and compared it to the results for the hyperbolic tangent profile (3.2). Slight changes in the film profile are not very important: as long as the lengthscale over which the temperature changes remains unchanged, the film profile and its stability properties remain nearly unchanged. Consequently, we focus only on the temperature profile given by (3.2). The height of

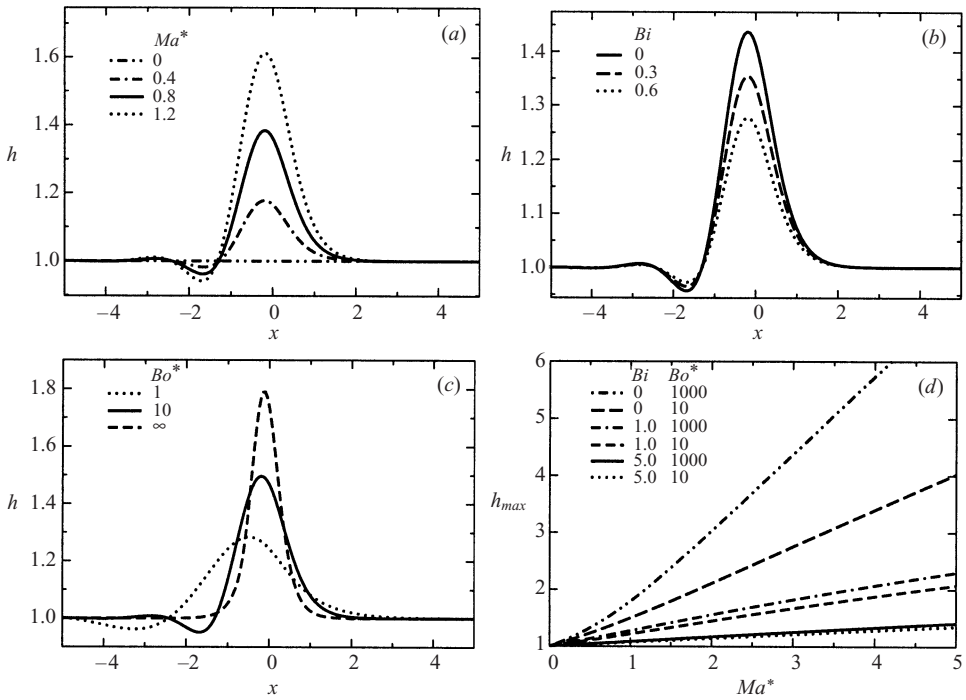

FIGURE 3. Film profiles for the steady solutions plotted parametrically (a) for different Ma^* with $Bo^* = 10$ and $Bi = 0$; (b) for different Bi, with $Ma^* = 1.0$ and $Bo^* = 10$; (c) for different Bo^*, with $Ma^* = 1.0$ and $Bi = 0$. (d) Maximum height as a function of Ma^*. For all plots $l/L = 20$.

the bump increases approximately linearly with Ma^* (figure 3a, d). Bi acts to reduce the effective temperature gradient at the film surface and results in a decrease of the bump height (see figure 3b). $1/Bo^*$ is the non-dimensional curvature pressure and its increase reduces the curvature and height of the steady solutions (see figure 3c). The upstream depressions are due to the influence of curvature pressure.

4. Linear stability analysis

To study the linear stability of the base-state solutions we use a perturbation of the form

$$h = h_0(x) + \epsilon h_1(x)\,\mathrm{e}^{\mathrm{i}ky+\beta t}, \tag{4.1}$$

where we are able to Fourier transform in the y-direction since the steady solution is invariant in that direction. Inserting equation (4.1) into (2.16) yields for $Bi = 0$ a linear differential equation with non-constant nonlinear coefficients:

$$\begin{aligned} 0 = &\left[\beta - Ma^*(h_0 T_{0x})_x + \frac{1}{Bo^*}(h_0^2 h_{0xxx})_x + 2h_0 h_{0x} + \frac{k^4}{3Bo^*}h_0^3\right] h_1 \\ &+ \left[\frac{1}{Bo^*}h_0^2(h_{0xxx} - k^2 h_{0x}) - Ma^* h_0 T_{0x} + h_0^2\right] h_{1x} \\ &- \frac{2k^2}{3Bo^*}h_0^3 h_{1xx} + \frac{1}{Bo^*}h_0^2 h_{0x} h_{1xxx} + \frac{1}{3Bo^*}h_0^3 h_{1xxxx}. \end{aligned} \tag{4.2}$$

We refer the reader to the Appendix for details of the case $Bi \neq 0$.

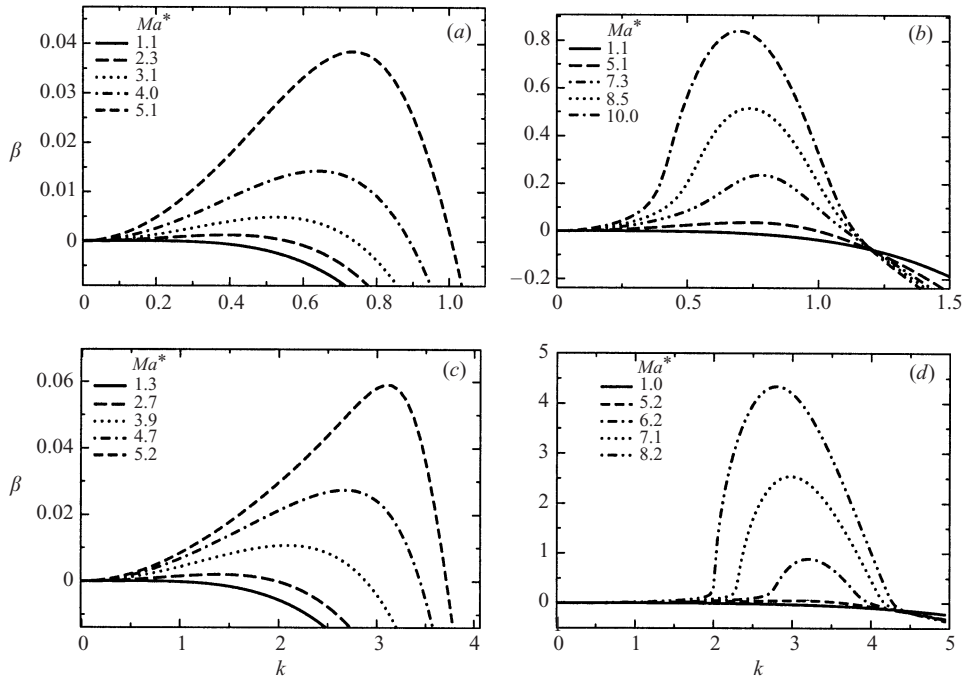

FIGURE 4. Dispersion relations showing the growth rate, β, versus the wavenumber, k, for (a) $Ma^* < 5$ and (b) $Ma^* < 10$ with $Bo^* = 10$, $Bi = 0$; dispersion relations for (c) $Ma^* < 5$ and (d) $Ma^* < 10$ with $Bo^* = 1000$, $Bi = 0$. For all plots $l/L = 20$.

In order to numerically solve equation (4.2) we discretize it by expressing the derivatives of $h_1[i]$ at a point i as a linear combination of $h_1[n]$ where $i-2 \leqslant n \leqslant i+2$. Using periodic boundary conditions this yields the algebraic eigenvalue problem:

$$\beta h_1 + \mathbf{L}(k, h_0, h_{0x}, h_{0xx}, h_{0xxx}, h_{0xxxx}, T_{0x}, T_{0xx})\, h_1 = 0, \tag{4.3}$$

where $\mathbf{L}$ is a linear operator that is determined by the base-state solution, h_0, the wavenumber in the y-direction, k, and the gradient of the temperature field at the plate, T_{0x}. We solve for the largest eigenvalue (i.e. growth rates), β, and the corresponding eigenvector, h_1. If a density of more than 10 points per unit length is used for discretization the results are independent of this number.

For $Bi = 0$ we plot dispersion relations (i.e. β as a function of k) parametrically as a function of the dimensionless group Ma^* in figure 4. From these plots it is clear that while the bump is stable for perturbations purely in the streamwise direction ($k = 0$), it is linearly unstable for some spanwise perturbations as $\beta > 0$ for a range of transverse wavenumbers, $0 < k < k_0$. Increasing Ma^* amplifies the growth rate of the most unstable mode, β_{max}, and increases k_0. For small Ma^* the wavenumber of the most unstable mode, k_{max}, increases with Ma^*; however, the opposite tendency is clear for larger Ma^* (see figure 4a, c vs. figure 4b, d and also figure 5). The same tendency is found for all the cases studied: k_{max} first increases and then decreases with rising Ma^*. Comparing figures 4(a, b) with 4(c, d) we see that a decrease in the effective surface tension results in larger β_{max} and larger k_{max} for comparable Ma^*. Some eigenfunctions for the most unstable mode are shown in figure 6.

For $Bi \neq 0$ (see figure 7) the base state is unstable for oscillatory perturbations, corresponding to complex eigenvalues, as well as the real mode discussed above for

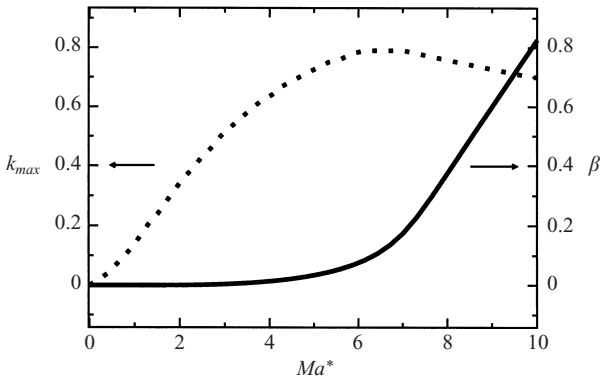

FIGURE 5. The wavenumber, k_{max}, and growth rate, β_{max}, of the most unstable mode for $Ma^* < 10$, $Bo^* = 10$, $Bi = 0$, $l/L = 20$.

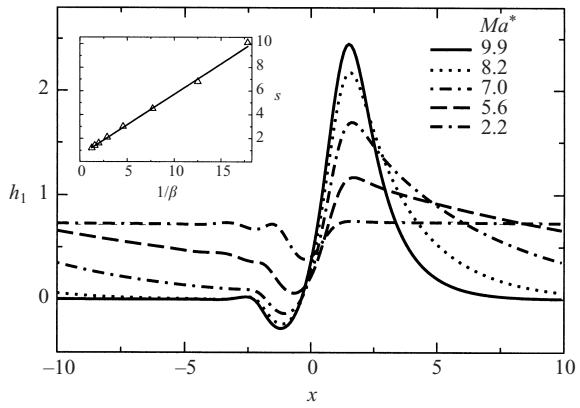

FIGURE 6. Eigenfunctions of the most unstable mode for $Bo^* = 10$, $Bi = 0$. Inset: distance from maximum to downstream half-maximum, s, versus growth timescale, $1/\beta$, for the eigenfunction of the most unstable mode for $Bo^* = 10$, $Bi = 0$, $l/L = 20$.

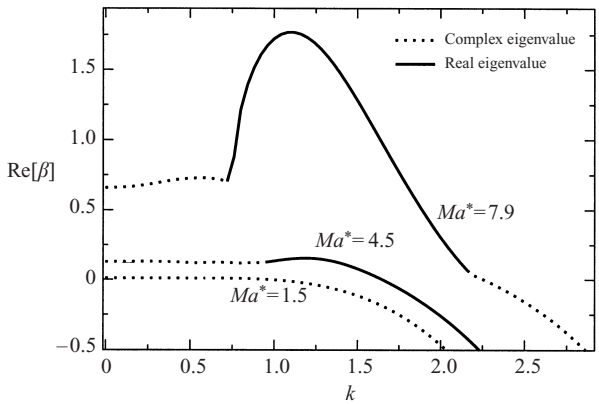

FIGURE 7. Dispersion results obtained from equation (A 1) for $Bo^* = 10$, $Bi = 0.1$, $l/L = 20$ plotted parametrically as a function of Ma^*. The transitions from solid to dotted lines represent the crossovers from the rivulet instability to a wavelike instability present in homogeneously heated falling films.

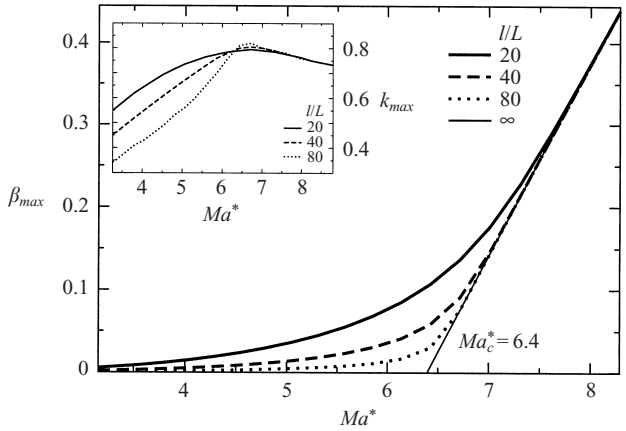

FIGURE 8. The growth rate for the most unstable mode, β_{max}, plotted parametrically for different domain lengths, l/L, with $Bo^* = 10$, $Bi = 0$. Also shown is the extrapolation for an infinite domain length. Inset: the equivalent for the wavenumber of the most unstable mode, k_{max}.

$Bi = 0$, which has a purely real eigenvalue. The oscillatory modes are similar in character to the unstable modes of a gravitationally driven flat falling film heated homogeneously (see the Appendix) and modes with no transverse dependence ($k = 0$) have a non-zero growth rate. Oscillatory modes are dominant for a certain range of k, which depends strongly on the periodicity of the array of heaters. For small Ma^* the most unstable mode can be oscillatory as the curve for $Ma^* = 1.5$ in figure 7 illustrates. For larger Ma^* the rivulet instability, identified by its purely real eigenvalues, is dominant. The eigenfunctions of the real mode are very similar to those for $Bi = 0$ (figure 6). Increasing Bi shifts dominance from the rivulet to the oscillatory instability. In the case $Bi = 0$ the oscillatory modes have relevance only for very small Ma^*. The real part of the growth rates of the oscillatory modes decreases as we increase the period of the array of heaters. Since we are most interested in the limiting case of a single heater (∞ period) we restrain our interest in the oscillatory modes and focus our attention on the localized real mode.

In order to understand the qualitatively different behaviours of the system for small and large Ma^* seen in figure 5 we study the shape of the eigenfunctions of the most unstable modes (see figure 6). As Ma^* decreases from 10 the eigenfunction becomes more elongated downstream and is no longer localized in the region of the steady-state bump. Decreasing Ma^* further extends the eigenfunction over the entire period. Physically, we expect the length of the downstream tail of the eigenfunction to correspond to the distance an instability is convected due to the base-state flow: the product of the timescale of the instability, $1/\beta$, and the velocity scale of the base state, $U_0 = 1$, is proportional to a characteristic downstream length of the eigenfunction. In the inset of figure 6 we see that the length between the maximum and downstream half-maximum of the eigenfunction, s, varies linearly with $1/\beta$. For smaller β, the length s becomes larger than the period of the array, implying that the delocalized eigenfunctions found for small Ma^* are due to the periodicity of the array.

5. Limit of one localized heater

To study the effect of the period length l and extrapolate the results to a single localized heater, we plot in figure 8 the maximum growth rate, β_{max}, and its associated

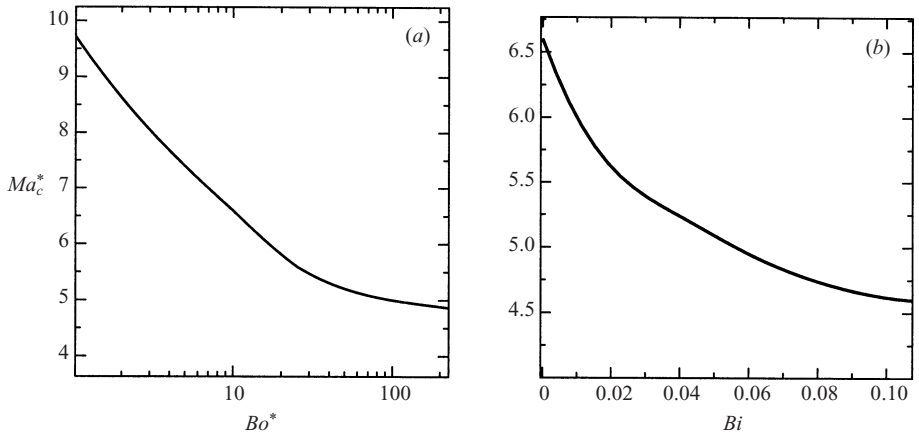

FIGURE 9. The critical Marangoni number, Ma_c^*, (a) as a function of the Bond number Bo^* with $Bi = 0$, (b) as a function of the Biot number Bi with $Bo^* = 10$.

wavenumber, k_{max}, as a function of Ma^* for different l. For localized eigenfunctions ($Ma^* \geqslant 7$) the results are independent of l, whereas for non-localized eigenfunctions ($Ma^* \leqslant 7$) β_{max} and k_{max} decrease with increasing l.

Upon increasing the size of the domain, we see the localized mode for smaller Ma^*. This supports the physical picture introduced above, namely that the behaviour in the region of smaller Ma^* is influenced by the periodicity of the array and that such an influence is destabilizing. In the region of localized eigenfunctions, β is a linear function of Ma^*. If one considers $l \to \infty$, the influence of periodicity would be eliminated and the case of a single localized heater recovered. However, such a numerical experiment is impossible using our methods. A reasonable assumption is that the linear behaviour found for localized eigenfunctions would continue since for an infinite period all eigenfunctions are localized. Extending the line of $\beta(Ma^*)$, we see that it crosses the x-axis at a point Ma_c^*, the critical Marangoni number for a single heater. The wavenumber of the most unstable mode at Ma_c^* approaches an asymptotic value, which we take as the wavenumber at onset, as the period length is increased. In this limit for $Ma^* < Ma_c^*$ all bumps are stable to transverse instabilities, while for $Ma^* > Ma_c^*$ we have a rivulet instability. In the experiment performed with a single heater (Scheid *et al.* 2000) the region where the wavenumber of the maximum unstable mode increases with Ma^* is not expected to exist because this is a behaviour characteristic of non-localized eigenfunctions.

Finally, we study the dependence of the critical Marangoni number on the parameters of the system, Bo^* and Bi. Ma_c^* decreases both with increasing the associated Bond number and with increasing the Biot number as shown in figure 9. It is well known that surface tension, measured in our system by the inverse of the associated Bond number, $1/Bo^*$, is stabilizing and has a greater stabilizing effect on shorter-wavelength perturbations (see equation (A 2)). This stabilizing effect is seen in the increase of the wavelength of the most unstable eigenfunction (see figure 4) as well as in the increase of the critical Marangoni number with decreasing Bo^* (see figure 9a). Increasing the Biot number is destabilizing (see figure 9b) since this allows for an additional thermocapillary instability mechanism.

Term	Expression	Physical mechanism
1	ch_{1x}	Convective flow in x-direction due to travelling wave reference velocity, c
2	$\frac{1}{3Bo^*}(h_0^3 h_{1xxx})_x$	Capillary flow in x-direction induced by perturbation curvature in x
3	$-\frac{1}{3Bo^*}(k^2 h_0^3 h_{1x})_x$	Capillary flow in x-direction induced by perturbation curvature in y
4	$(h_0^2 h_1)_x$	Flow in x-direction due to gravity
5	$\frac{1}{Bo^*}(h_0^2 h_{0xxx} h_1)_x$	Capillary flow in x-direction due to perturbation thickness variations
6	$-\frac{1}{3Bo^*}k^2 h_0^3 h_{1xx}$	Capillary flow in y-direction induced by perturbation curvature in x
7	$\frac{k^4 h_0^3 h_1}{3Bo^*}$	Capillary flow in y-direction induced by perturbation curvature in y
8	$-Ma^*(T_x^i h_0 h_1)_x$	Thermocapillary flow in x-direction due to perturbation thickness variations
9	$Ma^*\left[\frac{h_0^2}{2}\left(\frac{T^i Bi h_1}{1+Bi h_0}\right)_x\right]_x$	Thermocapillary flow in x-direction due to streamwise temperature variations
10	$-\frac{k^2 Bi Ma^* T^i h_0^2 h_1}{2(1+Bi h_0)}$	Thermocapillary flow in y-direction due to transverse temperature gradients

TABLE 3. Terms of the linear operator and their physical interpretation.

6. Instability mechanisms

Following Spaid & Homsy (1996), the growth rate β can be interpreted as an energy production rate, E^*, and a quadratic form can be used to calculate the contributions of the individual terms to this production rate. Equation (4.3) is multiplied by h_1 and integrated over one period in order to find the resulting individual contributions, β_n:

$$\beta_n = -\frac{\langle h_1, \mathbf{L}_n h_1 \rangle}{\langle h_1, h_1 \rangle}. \tag{6.1}$$

where

$$\langle v, w \rangle = \int_0^l vw \, \mathrm{d}x, \tag{6.2}$$

and the operators $\mathbf{L}_n$ are the individual terms of the linear operator $\mathbf{L}$, which depend nonlinearly on the base flow solution, $h_0(x)$, and are listed with their physical meaning in table 3. The interpretation in the literature is that terms of the linear operator corresponding to positive β_n are destabilizing, while terms corresponding to negative β_n are stabilizing (Spaid & Homsy 1996; Kataoka & Troian 1997, 1998). Using this interpretation we compare in table 4 the instability of a liquid ridge in a moving contact line with our system in the non-localized regime for $Ma^* < Ma_c^*$ and the localized regime for $Ma^* > Ma_c^*$ as shown in figure 10.

Various β_n are non-zero for $k = 0$ (see figure 10); however, they always balance to yield a transversely invariant neutrally stable state. Consequently, interpreting the results as in the literature does not reveal the instability mechanism. The destabiliza-

Term	Spaid & Homsy	Kataoka & Troian	Kataoka & Troian	$Bi = 0$	$Bi \neq 0$
1	None	None	None	NA	NA
2	Stabilizing	Destabilizing	Stabilizing	Stabilizing	Stabilizing
3	Stabilizing	Stabilizing	Stabilizing	Stabilizing	Stabilizing
4	Most destabilizing	NA	Stabilizing	Destabilizing	Destabilizing
5	Stabilizing	Stabilizing	Stabilizing	Most destabilizing	Destabilizing
6	Destabilizing	Destabilizing	Destabilizing	Destabilizing	Destabilizing
7	Stabilizing	Stabilizing	Stabilizing	Stabilizing	Stabilizing
8	NA	Most destabilizing	Most destabilizing	Stabilizing	Stabilizing
9	NA	NA	NA	NA	Destabilizing
10	NA	NA	NA	NA	Most destabilizing

TABLE 4. The effect of the various terms of the linear operator on the stability of moving contact lines (Spaid & Homsy 1996, figure 13; Kataoka & Troian 1997, figure 7; Kataoka & Troian 1998, figure 5) and stationary fluid ridges ($Bi = 0$, $Bi \neq 0$) using the interpretation of the energy analysis in the literature. If a term does not appear in one of the systems discussed NA (not applicable) is placed in the corresponding box.

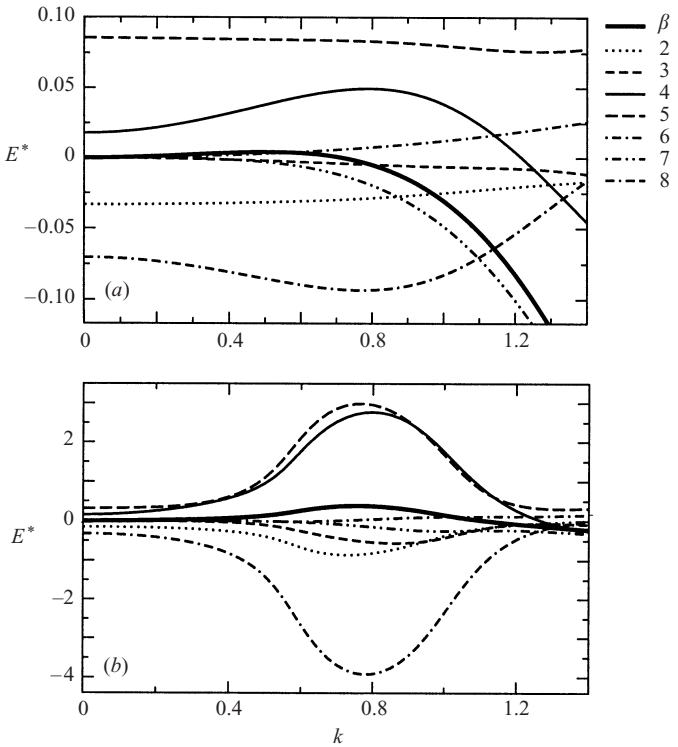

FIGURE 10. Contributions to the largest eigenvalue of the various terms of the operator plotted as a function of the wavenumber with $Bo^* = 10$, $Bi = 0$ and $l/L = 20$ in (a) the non-localized regime for $Ma^* = 3.0$ and (b) the localized regime for $Ma^* = 8.0$.

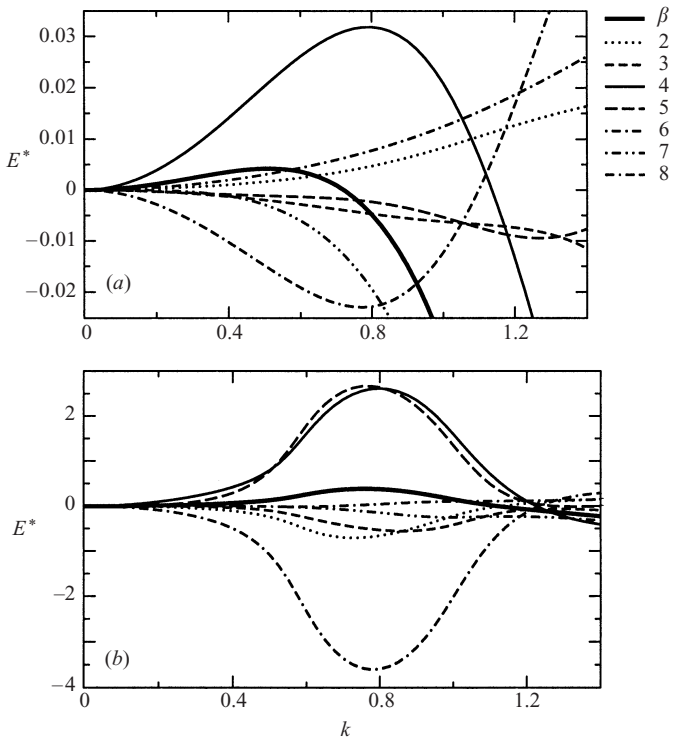

FIGURE 11. The contributions to the largest eigenvalue of the various terms of the operator relative to their contributions to the marginally stable state at $k = 0$ plotted as a function of the wavenumber with $Bo^* = 10$, $Bi = 0$ and $l/L = 20$ in (a) the non-localized regime for $Ma^* = 3.0$ and (b) the localized regime for $Ma^* = 8.0$.

tion of the marginally stable state arises as a result of deviations of the values of the β_n from their values at $k = 0$. Hence the most important instability mechanisms are those in which the associated β_n deviate most from their values at $k = 0$ as plotted in figure 11. We see that for $Bi = 0$ and $Ma^* < Ma_c^*$ term 5, which was previously interpreted as the most destabilizing is now a stabilizing factor. The non-localized and localized regimes for $Bi = 0$ are clearly distinguished by the roles of terms 2 and 5: term 2 changes from destabilizing to stabilizing, and term 5 changes from stabilizing to destabilizing as the Marangoni number is increased. At the onset of the instability gravity (term 4) acts with the capillary flow in the x-direction induced by perturbation thickness variations (term 5) to destabilize the flow. The maxima of the $\beta_4(k)$ and $\beta_5(k)$ shift with increasing Ma^* towards larger and smaller wavenumbers, respectively. The change in the relative destabilizing influence of the two terms causes the wavenumber of the fastest growing mode to increase with Ma^* in the non-localized regime and decrease with Ma^* in the localized regime. The $Bi = 0$ instability is different from the contact line instabilities because term 5 is crucially involved in the destabilization process. For the $Bi \neq 0$ case the main destabilizing mechanisms are thermocapillarity and gravity, thus making this another qualitatively different type of instability. In both the $Bi = 0$ and $Bi \neq 0$ fluid ridge instabilities analysed in this paper the main stabilizing influence is the thermocapillary flow in the x-direction.

In table 5 we summarize the effects of the terms as determined relative to their influence at $k = 0$. We note that this interpretation resolves some of the discrepancies

Term	Spaid & Homsy	Kataoka & Troian	Kataoka & Troian	$Bi = 0$	$Bi \neq 0$
1	None	None	None	NA	NA
2	Most destabilizing	Most destabilizing	None*	Stabilizing[1]	Destabilizing
3	Stabilizing	Stabilizing	Stabilizing	Stabilizing	Stabilizing
4	Destabilizing	NA	Most destabilizing	Destabilizing	Destabilizing
5	Stabilizing	Stabilizing	Stabilizing	Most destabilizing[2]	Stabilizing
6	Destabilizing	Destabilizing	Destabilizing	Destabilizing	Destabilizing
7	Stabilizing	Stabilizing	Stabilizing	Stabilizing	Stabilizing
8	NA	Destabilizing	Stabilizing	Stabilizing	Stabilizing
9	NA	NA	NA	NA	Destabilizing
10	NA	NA	NA	NA	Most destabilizing

TABLE 5. The effect of the various terms of the linear operator on the stability of moving contact lines (Spaid & Homsy 1996; Kataoka & Troian 1997, 1998) and stationay fluid ridges ($Bi = 0$, $Bi \neq 0$) using the new interpretation of the energy analysis. * The change in value of this term relative to its value at $k = 0$ is so small it can not be resolved by looking at the published results. If a term does not appear in one of the systems discussed NA (not applicable) is placed in the corresponding box. [1] Destabilizing for $Ma^* < Ma_c^*$; [2] stabilizing for $Ma^* < Ma_c^*$.

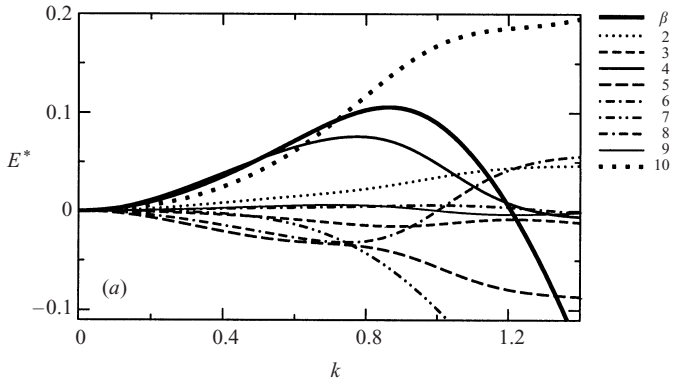

FIGURE 12. The contributions to the largest eigenvalue of the various terms of the operator relative to their contributions to the marginally stable state at $k = 0$ plotted as a function of the wavenumber with $Ma^* = 5.0$, $Bo^* = 4$, $Bi = 0.12$ and $l/L = 20$.

between the various physical systems found in table 4. Term 2, which was previously interpreted as destabilizing in Kataoka & Troian (1997) while being stabilizing in the other works on moving contact lines, is now interpreted as being destabilizing in all those systems.

7. Discussion

A comparison of the experimentally measured and theoretically computed shapes of the bump profiles before instability is shown in figure 13 for $Bo^* = 3.5$, $Bi = 0.12$, and $Ma^* = 1.09$ and 0.31. Since we do not have measurements of the surface temperature we must infer the experimental Marangoni number. We use the experimentally measured lengthscale of the bump to determine Bo^*. For the experimentally deter-

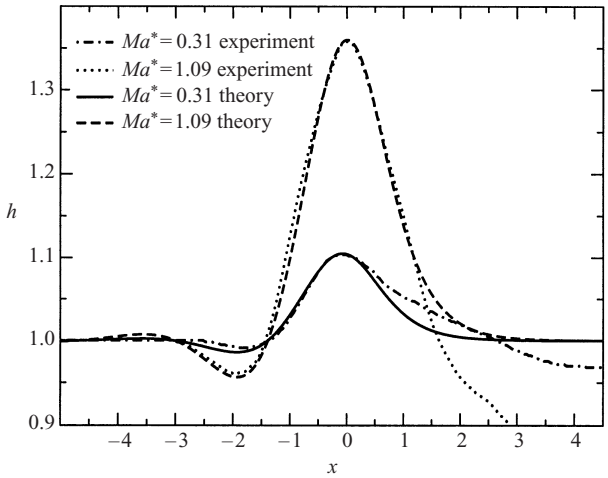

FIGURE 13. Comparison of experiment ($Re = 0.27$ and 25% ethyl achohol) and theory for $Bo^* = 3.5$, $Bi = 0.12$ and $l/L = 20$.

			Ma_c^*		k_c	
Bo^*	Bi	Re	Experimental	Theoretical	Experimental	Theoretical
3.5	0.12	0.27	1.2 ± 0.1	5.79	No data	0.90
2.5	0.14	0.39	1.4 ± 0.1	6.20	0.88	0.83
2.0	0.16	0.75	1.45 ± 0.15	6.52	1.18	0.80
2.0	0.21	1.5	1.1 ± 0.1	6.40	1.08	0.87

TABLE 6. Comparison of the experimental and theoretical critical Marangoni number, Ma_c^*, and the wavenumber at the onset of instability, k_c. The theoretical calculation is independent of the Reynolds number. The Biot and Bond numbers are the same for both experiment and theory.

mined Bo^* and Bi, we calculate theoretically the maximum height as a function of Ma^*. We take the experimental Marangoni number to be where this height matches the experimentally measured maximum height. The theoretical and experimental profiles are in excellent agreement: all the main features of the experimental profile, such as the upstream depression due to curvature pressure, are present in the computed profile. We note that the thickness of the experimental profile decreases from 1 after the bump due to cumulative errors in the integration technique used to measure the bump profile in the experiment.

Considering only the regime of localized eigenfunctions, we compare our model with the experimental observations for one localized heater (Kabov & Chinnov 1997; Scheid *et al.* 2000). The wavenumber at the onset of instability found theoretically is in quantitative agreement with the experimentally observed values (see table 6). The average deviation between the two values is 20%. Above the instability threshold, the model predicts that the wavenumber of the most unstable mode, k_{max}, decreases with Ma^* (see figure 5), which is in qualitative agreement with experimental observations (Kabov *et al.* 1996). It is worth noting that for a homogeneously heated falling film the wavenumber of the most unstable mode scales as $Ma^{*1/2}$ (see the Appendix). In contrast, the most unstable wavenumber past onset for the stationary fluid ridges studied in this paper decreases with increasing Ma^*. The order of magnitude of the

critical Ma^* is also in agreement with experiment; however, the prediction is 5 times higher than the experimentally obtained value (see table 5).

We have focused on low-Reynolds number flows with a small aspect ratio ϵ. Our theory applies to the thinner films used in the experiment; however, the lubrication limit begins to break down for the thicker experimental films ($\approx 100\,\mu$m). This may account for the increasing deviation between the experimental and theoretical values of the critical Marangoni number with increasing Re (see table 5). Further experimental and theoretical investigation will be needed to elucidate this issue.

8. Conclusion

The intent of this study has been to develop an understanding of the mechanisms by which a falling film on a locally heated plate loses stability. After a short discussion of the experimental results used as a basis for constructing our model we derived an evolution equation for the film thickness. Its stationary solutions and their stability were calculated numerically for an array of heaters. By considering the large-period limit for the array we recovered the single heater case. The results elucidate the influence of temperature-gradient-induced surface tension gradients, curvature pressure, gravity and heat conduction on the shape of the steady flow profile and its stability. Our results are in quantitative (film profile, observed wavelength at the onset of the instability) and qualitative (critical Marangoni number, dependence of observed wavenumber on the Marangoni number) accord with existing experimental results (Kabov 1996; Kabov & Chinnov 1997; Kabov 1998; Scheid *et al.* 2000). We find that the interaction of base-state curvature with perturbation thickness, gravity and thermocapillarity (only in the case $Bi \neq 0$) all play important roles in destabilizing the fluid ridge. Consequently, the studied liquid ridge instability is different in character from instabilities of driven contact lines.

The authors would like to thank P. Colinet, O. A. Kabov, J. C. Legros, K. Neuffer, A. Ridha, V. M. Starov, M. G. Velarde, R. K. Zeytounian and E. Knobloch for helpful discussions. This work was funded by the Fulbright comision, the Spanish Ministry of Education and Culture under grant PB 96-599, the European Union under ICOPAC grant HPRN-CT-2000-00136, COPERNICUS grant ERB IC15-CT98-0908 and by the German Academic Exchange Board (DAAD) under grant D/98/14745.

Appendix. Linear stability analysis for $Bi \neq 0$

Inserting equation (4.1) into (2.16) yields for $Bi \neq 0$ the linear differential equation

$$\beta h_1 + \frac{(h_0^3 h_{1xxx})_x}{3Bo^*} - \frac{(k^2 h_0^3 h_{1x})_x}{3Bo^*} + (h_0^2 h_1)_x + \frac{(h_0^2 h_{0xxx} h_1)_x}{Bo^*} - \frac{k^2 h_0^3 h_{1xx}}{3Bo^*} + \frac{k^4 h_0^3 h_1}{3Bo^*}$$
$$- Ma^* (T_x^i h_0 h_1)_x + Ma^* \left[\frac{h_0^2}{2} \left(\frac{T^i Bi h_1}{1 + Bi h_0} \right)_x \right]_x - \frac{BiMa^* k^2 T^i h_0^2 h_1}{2(1 + Bi h_0)} = 0. \quad \text{(A 1)}$$

To better understand the influence of Ma^*, Bo^* and Bi we consider the simplified case of the stability of a flat film falling down a homogeneously heated plate (i.e. $h_0 = 1$, $T_0 = 1$). Note that ΔT and L no longer have the natural experimental scalings given in table 2 and the related non-dimensional groups would need to be adjusted

accordingly. Assuming variation in the x-direction takes the form $h_1 = e^{iqx}$ we find

$$\beta = -iq + |\boldsymbol{k}|^2 \left[\frac{BiMa^*}{2(1+Bi)^2} - \frac{|\boldsymbol{k}|^2}{3Bo^*} \right], \tag{A 2}$$

where $\boldsymbol{k}$ is the vector (q,k). Equation (A 2) can be solved for the wavenumber of the most unstable mode:

$$|\boldsymbol{k}|_c = \left[\frac{3BiBo^*Ma^*}{4(1+Bi)^2} \right]^{1/2}. \tag{A 3}$$

The non-dimensional curvature pressure acts to stabilize large-wavenumber perturbations while the influence of the Biot number is destabilizing. For $Bi \neq 0$ the film is always unstable for small wavenumbers. Consider a wavelike perturbation on a film with $Bi \neq 0$: the surface now further from the plate will be cooler and the surface tension will increase locally; the surface closer to the plate is warmed, which results in a decrease in surface tension. The concomitant flow, driven by the gradients in surface tension, is away from the valleys and towards the peaks thus further destabilizing the film (Scriven & Sternling 1964; Smith 1966). Gravity, responsible for the imaginary part of β, causes wave motion. This form of wavelike instability is also found in numerical solutions of equation (A 1) for the case with a temperature jump as considered here. For $Bi = 0$, the real part of the growth rate is always less than or equal to zero and the homogeneously heated film is stable (see equation (A 2)).

REFERENCES

Bertozzi, A. L. & Brenner, M. P. 1997 Linear stability and transient growth in driven contact lines. *Phys. Fluids* **9**, 530–539.

Bertozzi, A. L., Münch, A., Fanton, X. & Cazabat, A. M. 1998 Contact line stability and 'undercompressive shocks' in driven thin film flow. *Phys. Rev. Lett.* **81**, 5169–5173.

Doedel, E., Champneys, A., Fairfrieve, T., Kuznetsov, Y., Sandstede, B. & Wang, X. 1997 *AUTO97: Continuation and Bifurcation Software for Ordinary Differential Equations*. Montreal: Concordia University.

Eres, M., Schwartz, L. & Roy, R. 2000 Fingering phenomena for driven coating films. *Phys. Fluids* **12**, 1278–1295.

Hosoi, A. E. & Mahadevan, L. 1999 Axial instability of a free-surface front in a partially filled horizontal rotating cylinder. *Phys. Fluids* **11**, 97–106.

Ito, A., Masunaga, N. & Baba, K. 1995 Marangoni effects on wave structure and liquid film breakdown along a heated vertical tube. *Advances in Multiphase Flow* (ed. A. Serizawa, T. Fukano & J. Bataille), pp. 255–265. Elsevier.

Ji, W. & Setterwall, F. 1994 On the instabilities of vertical falling liquid films in the presence of surface-active solute. *J. Fluid Mech.* **278**, 297–323.

Joo, S., Davis, S. H. & Bankoff, S. 1991 Long-wave instabilities of heated films: two dimensional theory of uniform layers. *J. Fluid Mech.* **230**, 117–146.

Joo, S., Davis, S. H. & Bankoff, S. 1996 A mechanism for rivulet formation in heated films. *J. Fluid Mech.* **321**, 279–298.

Kabov, O. A. 1994 Heat transfer from a heater with a small linear dimension to a free falling liquid film. In *Proc. 1st Russian National Conf. on Heat Transfer*, vol. 6, pp. 90–95. Moscow Institute of Energy.

Kabov, O. A. 1996 Heat transfer from a small heater to a falling liquid film. *Heat Transfer Res.* **27**(1–4), 221–226.

Kabov, O. A. 1998 Formation of regular structures in a falling liquid film upon local heating. *Thermophys. Aeromech.* **5**, 547–551.

Kabov, O. A. & Chinnov, E. 1997 Heat transfer from a local heat source to a subcooled falling liquid film evaporating in a vapor-gas medium. *Russ. J. Engng Thermophys.* **7**, 1–34.

KABOV, O. A., MARCHUK, I. V. & CHUPIN, V. M. 1996 Thermal imaging study of a liquid film flowing on a vertical surface with a local heat source. *Russ. J. Engng Thermophys.* **6**(2), 105–138.

KALLIADASIS, S., BIELARZ, C. & HOMSY, G. M. 2000 Steady free-surface thin film flows over topography. *Phys. Fluids* **12**, 1889–1898.

KALLIADASIS, S. & HOMSY, G. M. 2001 Stability of free-surface thin film flows over topography. *J. Fluid Mech.* **448**, 387–410.

KATAOKA, D. & TROIAN, S. 1997 A theoretical study of instabilities at the advancing front of thermally driven coating films. *J. Colloid Interface Sci.* **192**, 350–362.

KATAOKA, D. & TROIAN, S. 1998 Stabilizing the advancing front of thermally driven climbing films. *J. Colloid Interface Sci.* **203**, 335–344.

KELLEY, R., DAVIS, S. & GOUSSIS, D. 1986 On the instability of a heated film flow with variable surface tension. *Proc. 8th Intl Heat Transfer Conf.*, vol. 4, pp. 1937–1942.

LIN, S. 1974 Finite amplitude side-band instability of a viscous film. *J. Fluid Mech.* **63**, 417–429.

MOYLE, D., CHEN, M. & HOMSY, G. 1999 Nonlinear rivulet dynamics during unstable wetting flows. *Intl J. Multiphase Flow* **12**, 1243–1262.

ORON, A., DAVIS, S. H. & BANKOFF, S. G. 1997 Long-scale evolution of thin liquid films. *Rev. Mod. Phys.* **69**, 931–980.

ORON, A. & ROSENAU, P. 1992 Formation of patterns induced by thermocapillarity and gravity. *J. Phys.* II *Paris* **2**, 131–146.

PEREZ CORDON, R. & VELARDE, M. 1975 On the (non-linear) foundations of Boussinesq approximation applicable to a thin layer of fluid. *J. Phys. Paris* **36**, 591–601.

SCHEID, B., KABOV, O., MINETTI, C., COLINET, P. & LEGROS, J. 2000 Measurement of free surface deformation by reflectance-Schlieren method. In *Proc. 3rd Eur. Conf. Heat Mass Transfer, Heidelberg*.

SCRIVEN, L. E. & STERNLING, C. V. 1964 On cellular convection driven by surface-tension gradients: effects of mean surface tension and surface viscosity. *J. Fluid Mech.* **19**, 321–340.

SMITH, K. 1966 On convective instability induced by surface-tension gradients. *J. Fluid Mech.* **24**, 401–414.

SPAID, N. & HOMSY, G. 1996 Stability of Newtonian and viscoelastic dynamic contact lines. *Phys. Fluids* **8**, 460–478.

SREENIVASAN, S. & LIN, S. P. 1978 Surface tension driven instability of a liquid film flow down a heated incline. *Intl J. Heat Mass Transfer* **21**, 1517–1526.

TROIAN, S., HERBOLZHEIMER, E., SAFRAN, S. & JOANNY, J. 1989 Fingering instabilities of driven spreading films. *Europhys. Lett.* **10**, 25–30.

ZEYTOUNIAN, R. 1998 The Benard–Marangoni thermocapillary-instability problem. *Phys. Uspekhi* **168**(3), 259–286.